Research Article | Vol. 8, No. 3 | 1 Mar 2017 | BIOMEDICAL OPTICS EXPRESS 1763

Biomedical Optics EXPRESS

Measurement of multispectral scattering properties in mouse brain tissue

EUNJUNG MIN,[1,2,6] SUNGBEA BAN,[1,6] YANYAN WANG,[3] SUNG CHUL BAE,[1] GABRIEL POPESCU,[2] CATHERINE BEST-POPESCU,[4,7] AND WOONGGYU JUNG[1,5,8]

[1]*Department of Biomedical Engineering, Ulsan National Institute of Science and Technology (UNIST), Ulsan, South Korea*
[2]*Quantitative Light Imaging Laboratory, Department of Electrical and Computer Engineering, Beckman Institute for Advanced Science and Technology, University of Illinois at Urbana-Champaign, Urbana, IL 61801, USA*
[3]*Department of Pharmacology and Beckman Institute, University of Illinois at Urbana-Champaign (UIUC), Urbana, IL 61801, USA*
[4]*Cellular Neuroscience and Imaging Laboratory, Department of Bioengineering, University of Illinois at Urbana-Champaign, Urbana, IL 61801, USA*
[5]*Center for Soft and Living Matter, Institute for Basic Science (IBS), Ulsan, South Korea*
[6]*These authors contributed equally to this work*
[7]*cabest@illinois.edu*
[8]*wgjung@unist.ac.kr*

Abstract: We present the scattering properties of mouse brain using multispectral diffraction phase microscopy. Typical diffraction phase microscopy was incorporated with the broadband light source which offers the measurement of the scattering coefficient and anisotropy in the spectral range of 550-900 nm. The regional analysis was performed for both the myeloarchitecture and cytoarchitecture of the brain tissue. Our results clearly evaluate the multispectral scattering properties in the olfactory bulb and corpus callosum. The scattering coefficient measured in the corpus callosum is about four times higher than in the olfactory bulb. It also indicates that it is feasible to realize the quantitative phase microscope in near infrared region for thick brain tissue imaging.

© 2017 Optical Society of America

OCIS codes: (180.3170) Interference microscopy; (120.5050) Phase measurement; (160.4760) Optical properties; (290.5820) Scattering measurements; (110.3080) Infrared imaging.

References and links

1. O. Sporns, G. Tononi, and R. Kötter, "The human connectome: A structural description of the human brain," PLOS Comput. Biol. **1**(4), e42 (2005).
2. P. E. Roland and K. Zilles, "Brain atlases--a new research tool," Trends Neurosci. **17**(11), 458–467 (1994).
3. A. W. Toga, P. M. Thompson, S. Mori, K. Amunts, and K. Zilles, "Towards multimodal atlases of the human brain," Nat. Rev. Neurosci. **7**(12), 952–966 (2006).
4. A. de Crespigny, H. Bou-Reslan, M. C. Nishimura, H. Phillips, R. A. Carano, and H. E. D'Arceuil, "3D micro-CT imaging of the postmortem brain," J. Neurosci. Methods **171**(2), 207–213 (2008).
5. H. Wei, L. Xie, R. Dibb, W. Li, K. Decker, Y. Zhang, G. A. Johnson, and C. Liu, "Imaging whole-brain cytoarchitecture of mouse with MRI-based quantitative susceptibility mapping," Neuroimage **137**, 107–115 (2016).
6. T. Ragan, L. R. Kadiri, K. U. Venkataraju, K. Bahlmann, J. Sutin, J. Taranda, I. Arganda-Carreras, Y. Kim, H. S. Seung, and P. Osten, "Serial two-photon tomography for automated ex vivo mouse brain imaging," Nat. Methods **9**(3), 255–258 (2012).
7. A. Li, H. Gong, B. Zhang, Q. Wang, C. Yan, J. Wu, Q. Liu, S. Zeng, and Q. Luo, "Micro-optical sectioning tomography to obtain a high-resolution atlas of the mouse brain," Science **330**(6009), 1404–1408 (2010).
8. K. Amunts, C. Lepage, L. Borgeat, H. Mohlberg, T. Dickscheid, M.-É. Rousseau, S. Bludau, P.-L. Bazin, L. B. Lewis, A.-M. Oros-Peusquens, N. J. Shah, T. Lippert, K. Zilles, and A. C. Evans, "BigBrain: an ultrahigh-resolution 3D human brain model," Science **340**(6139), 1472–1475 (2013).
9. G. Popescu, *Quantitative Phase Imaging of Cells and Tissues* (McGraw Hill Professional, 2011).
10. Y. Cotte, F. Toy, P. Jourdain, N. Pavillon, D. Boss, P. Magistretti, P. Marquet, and C. Depeursinge, "Marker-free phase nanoscopy," Nat. Photonics **7**(2), 113–117 (2013).

#282487 https://doi.org/10.1364/BOE.8.001763
Journal © 2017 Received 8 Dec 2016; revised 10 Feb 2017; accepted 14 Feb 2017; published 23 Feb 2017

Biomedical Optics EXPRESS

11. P. Marquet, B. Rappaz, P. J. Magistretti, E. Cuche, Y. Emery, T. Colomb, and C. Depeursinge, "Digital holographic microscopy: a noninvasive contrast imaging technique allowing quantitative visualization of living cells with subwavelength axial accuracy," Opt. Lett. **30**(5), 468–470 (2005).
12. C. Joo, T. Akkin, B. Cense, B. H. Park, and J. F. de Boer, "Spectral-domain optical coherence phase microscopy for quantitative phase-contrast imaging," Opt. Lett. **30**(16), 2131–2133 (2005).
13. B. Bhaduri, C. Edwards, H. Pham, R. Zhou, T. H. Nguyen, L. L. Goddard, and G. Popescu, "Diffraction phase microscopy: principles and applications in materials and life sciences," Adv. Opt. Photonics **6**(1), 57–119 (2014).
14. M. Lee, E. Lee, J. Jung, H. Yu, K. Kim, J. Yoon, S. Lee, Y. Jeong, and Y. Park, "Label-free optical quantification of structural alterations in Alzheimer's disease," Sci. Rep. **6**, 31034 (2016).
15. Z. Wang, L. Millet, M. Mir, H. Ding, S. Unarunotai, J. Rogers, M. U. Gillette, and G. Popescu, "Spatial light interference microscopy (SLIM)," Opt. Express **19**(2), 1016–1026 (2011).
16. E. Min, M. E. Kandel, C. J. Ko, G. Popescu, W. Jung, and C. Best-Popescu, "Label-free, multi-scale imaging of ex-vivo mouse brain using spatial light interference microscopy," Sci. Rep. **6**, 39667 (2016).
17. G. Popescu, T. Ikeda, R. R. Dasari, and M. S. Feld, "Diffraction phase microscopy for quantifying cell structure and dynamics," Opt. Lett. **31**(6), 775–777 (2006).
18. G. Popescu, Y. Park, W. Choi, R. R. Dasari, M. S. Feld, and K. Badizadegan, "Imaging red blood cell dynamics by quantitative phase microscopy," Blood Cells Mol. Dis. **41**(1), 10–16 (2008).
19. Z. Wang, H. Ding, and G. Popescu, "Scattering-phase theorem," Opt. Lett. **36**(7), 1215–1217 (2011).
20. H. Ding, Z. Wang, X. Liang, S. A. Boppart, K. Tangella, and G. Popescu, "Measuring the scattering parameters of tissues from quantitative phase imaging of thin slices," Opt. Lett. **36**(12), 2281–2283 (2011).
21. Z. Wang, K. Tangella, A. Balla, and G. Popescu, "Tissue refractive index as marker of disease," J. Biomed. Opt. **16**(11), 116017 (2011).
22. S. L. Jacques, "Optical properties of biological tissues: a review," Phys. Med. Biol. **58**(11), R37–R61 (2013).
23. H. Ding, Z. Wang, F. Nguyen, S. A. Boppart, and G. Popescu, "Fourier transform light scattering of inhomogeneous and dynamic structures," Phys. Rev. Lett. **101**(23), 238102 (2008).
24. H. Ding, F. Nguyen, S. A. Boppart, and G. Popescu, "Optical properties of tissues quantified by Fourier-transform light scattering," Opt. Lett. **34**(9), 1372–1374 (2009).
25. N. G. Horton, K. Wang, D. Kobat, C. G. Clark, F. W. Wise, C. B. Schaffer, and C. Xu, "In vivo three-photon microscopy of subcortical structures within an intact mouse brain," Nat. Photonics **7**(3), 205–209 (2013).
26. G. Hong, S. Diao, J. Chang, A. L. Antaris, C. Chen, B. Zhang, S. Zhao, D. N. Atochin, P. L. Huang, K. I. Andreasson, C. J. Kuo, and H. Dai, "Through-skull fluorescence imaging of the brain in a new near-infrared window," Nat. Photonics **8**(9), 723–730 (2014).
27. R. Kawakami, K. Sawada, A. Sato, T. Hibi, Y. Kozawa, S. Sato, H. Yokoyama, and T. Nemoto, "Visualizing hippocampal neurons with in vivo two-photon microscopy using a 1030 nm picosecond pulse laser," Sci. Rep. **3**, 1014 (2013).

1. Introduction

The human brain contains roughly 10^{12} neurons, which together result in an estimated 10^{15} connections [1]. This level of interconnectivity makes the brain the most complex machine known to mankind. Recovering a complete picture of all the neuronal connections in the brain, the *Connectome*, represents a formidable challenge for the imaging field. Routine clinical tools such as MRI and PET have the ability to image the brain *in vivo* [2, 3]. However, the resolution is limited to approximately 1 mm and the contrast without labels is not always optimal. Although the resolution limit spans to a few tens of microns in microCT and MRI for *ex vivo* brain imaging, the technologies are time-consuming, and the resolution and contrast are not sufficient to visualize cellular structure [4, 5]. Optical imaging, on the other hand, can extract information with submicron resolution. The limitation in this case is penetration depth, which is capped by the transport mean free path of the tissue. As a result, the main approach for imaging brain structures with high resolution over large depths is to section the tissue into micron thin slices, image each slice, and then to stitch the resulting images [6–8]. Because the slices of tissues exhibit low contrast under visible light illumination, imaging procedures involve staining or fluorescence tagging. While contrast labels boost the contrast significantly, the resulting image only reports on the presence of the tag itself, i.e., it provides an incomplete picture of the tissue structure. Furthermore, the information is qualitative and often altered by external factors, such as the quality of the preparation.

Quantitative phase imaging (QPI) [9] has been developed in response to the need for label-free, intrinsic contrast imaging, as well as quantitative information about the tissue

Biomedical Optics EXPRESS

structure. While a number of QPI approaches for visualizing neurons and brain tissues have been introduced, e.g., digital holographic microscopy [10, 11], optical coherence phase microscopy [12], diffraction phase microscopy (DPM) [13, 14], spatial light interference microscopy [15, 16], they all utilize interferometry as the underlying operating principle. From the interferogram, the alteration in optical pathlength due to tissue is obtained with nanoscale sensitivity. This level of sensitivity is difficult to achieve with any other method. However, QPI has been limited to visualizing cultured neurons and very thin histological section (4-5 microns) [10–16]. The reason is that the light scattering prevents imaging thick tissues.

Here we use multispectral DPM (MS-DPM) to image unlabeled brain slices. DPM [13, 17] is a particular type of QPI method, of very high stability, granted by the common-path interferometric geometry. Due to its intrinsic temporal sensitivity to phase changes, DPM is used in biomedical applications for measuring cell dynamics [18] and brain imaging [14]. In order to expand its applicability to thick sections, we developed a system that operates with multispectral bands including near infrared (NIR) illumination. In order to demonstrate the effect of scattering in NIR, scattering properties associated with tissue at different wavelengths across visible to NIR were measured and compared. The results show quantitatively the boost in tissue penetration provided by infrared vs. visible light.

2. Materials and method

2.1 Sample preparation

Histological sections of the mouse brain were prepared according to standard procedures. The brain was fixed in 4% paraformaldehyde for 24 hours at 4°C, and dehydrated through graded ethanol and xylene, and infiltrated with paraffin wax. It was then embedded in paraffin and sectioned along the coronal plane. All animal procedures were carried out in accordance with the recommendations in the Guide for the Care and Use of Laboratory Animals of the National Institutes of Health. The animal protocol was approved by the University of Illinois Animal Care and Use Committee (IACUC). Prior to imaging, the paraffin was completely removed by washes with xylene and graded ethanol.

2.2 Imaging

The schematic of MS-DPM system is illustrated in Fig. 1, which is a common-path, off-axis geometry. MS-DPM was built as an add-on module to a standard bright field microscope, designed to take information of phase differences from the specimen and surrounding mounting medium. In order to quantify the benefit of using NIR illumination, we developed a DPM system operated at a wide range of wavelengths, from the visible range to NIR. Specifically, we used a white light laser (Fianium, WhiteLase SC-400) as an illumination light source. For wavelength selection, optical filters (Delta optical thin film, LVNIRBP) were placed after the laser, which filter the wavelengths from 550 to 900 nm with a bandwidth of 6-14 nm. For the bright field microscope, we used a 40 × objective lens (OL, Olympus, UMPlanFl NA 0.8) and a 200 mm tube lens (Thorlabs, ITL200). For DPM, the diffraction grating (G) (Edmond, 92 grooves/mm) was placed at the image plane of the bright field microscope. The image field is divided by diffraction orders. The 0th and 1th order were used as reference and sample beam, respectively. The two beams pass through the first lens (L1) and only the 0th beam is spatially filtered by the pinhole (P), of 50 μm radius, placed at the Fourier plane (FP). The reference and sample beams are collected by the second lens (L2) such that they interfere at the EMCCD (Andor, iXon3). The obtained interference pattern was processed as described in [13]. The phase temporal and spatial stability of the system were measured to be 50 mrad and 40 mrad, respectively. The transverse resolution was 1.2 μm at the wavelength of 550 nm, and acquisition time was 30 frames/sec.

Biomedical Optics EXPRESS

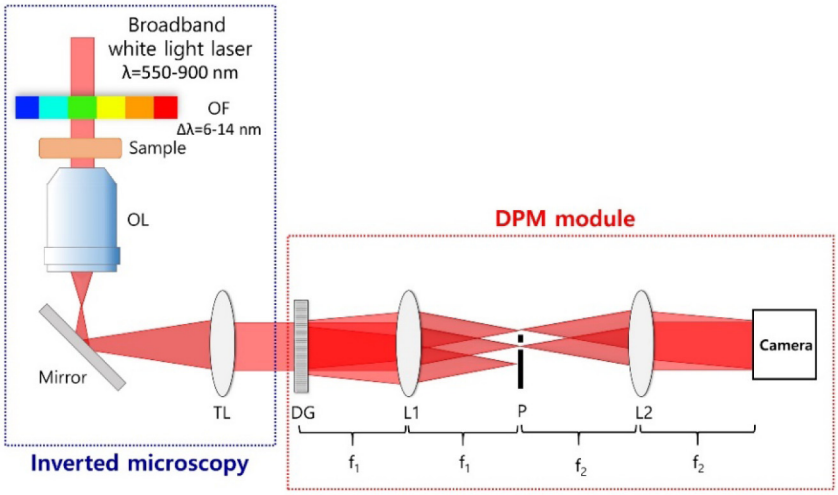

Fig. 1. Schematic of multispectral diffraction phase microscopy (MS-DPM). The DPM module is attached to the inverted bright field microscopy. The optical light source has multiple spectral bands. The broadband light source passes through optical filter (OF) that has tuning range of 550-900 nm and bandwidth of 6-14 nm. The light is scattered by tissue sample and collected by objective lens (OL). Off-axis geometric DPM module is equipped after image plane of bright field microscope, which is composed of diffraction grating (DG), two lenses (L1 and L2) having focal length of f_1 and f_2, pinhole (P) and camera. The diffraction grating is placed at the image plane that equal to the focal plane of tube lens (TL). In DPM module, the image field is interfered with plane wave and the interference pattern is detected with camera.

3. Result

MS-DPM images of the olfactory bulb region (anterior brain) were obtained at wavelengths spanning 550-900 nm as shown in Fig. 2(a). The olfactory bulb has a multi-layered structure. We imaged one cell layer containing a large number of cell bodies having high refractive index membranes and various organelles. For all of the different wavelengths, the phase images were converted to optical path length. The field of view and pixel sampling are 114 × 114 μm^2 (392 × 392 pixels) and 0.29 μm pixel, respectively. From the MS-DPM data, the scattering coefficient (μ_s) (Fig. 2) was calculated using the scattering-phase theorem as [19].

$$\mu_s = \frac{\left\langle \Delta \varnothing^2(r) \right\rangle_r}{L}$$

In Eq, $\left\langle \Delta \varnothing^2(r) \right\rangle_r$ indicates spatial variance of the phase and L is the thickness of the brain slice. Thus, the optical properties can be obtained using the phase information in a spatially resolved manner [20, 21]. The window size for the calculation was 2.9 × 2.9 μm^2. The result shows that the variance of phase decreases as expected at longer wavelength, thus the structure of tissue is relatively more transparent in the infrared illumination than in visible. According to the scattering-phase theorem, the scattering coefficient is proportional to the phase variance, which means the scattering is reduced at longer wavelengths, as shown in the graphs of Fig. 2(a). The absolute value of the scattering coefficient was fitted to the power law curve, $\sim a(\lambda/550\ \text{nm})^{-b}$, where scaling factor, a is scattering coefficient measured at wavelength of 550 nm and b is scattering power [22]. We performed the fit for spectral regions from visible (550-700 nm) to NIR (700-900 nm). As a result, the scattering power value was measured to be 3.28. The scattering coefficient at 550 nm is 5.45 times higher than one at 900 nm.

Biomedical Optics EXPRESS

The μ_s values were calculated for the local regions where axons, dendrites, and cell bodies were present. These values were plotted as a function of wavelength as shown in Figs. 2(b) and 2(c). Interestingly, we found that the optical property of tissue can be explained by the unit of the neuron component being imaged. In the graph, the scattering power in the axon/dendrites is slightly larger than in cell body. However, the mean and variance of the μ_s are noticeably higher in cell body [Fig. 2(c)] compared to axons and dendrites [Fig. 2(b)]. Thus, the wide range of the optical property value analyzed in Fig. 2(a) can be explained by the different phase variance and μ_s of each respective graph. In other words, the optical properties of specific regions with respect to wavelength depend strongly on neural components. The p-value ($< 10^{-2}$) between the graphs of Figs. 2(b) and 2(c) shows that the optical property is able to act as a parameter for classifying brain tissue.

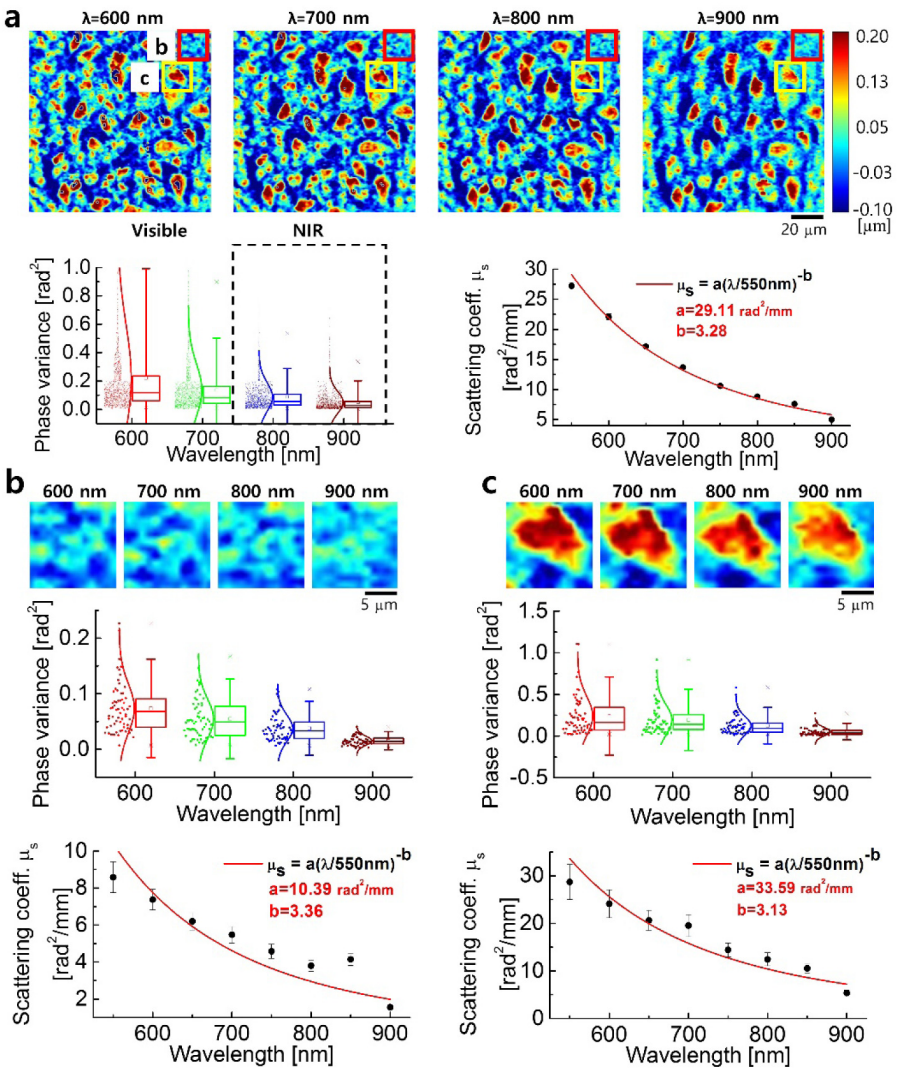

Fig. 2. Measurement of the scattering coefficient in the olfactory bulb using MS-DPM data. Phase variance and scattering coefficient obtained in the region of olfactory bulb and its subregions (a): axon/dendrites (b) and cell body (c). The phase variance is plotted using box plot. The box covers the 25–75% percentiles, and the maximum length of whisker is 2 times the standard deviation. The scattering coefficient is measured by using scattering-phase theorem, as described in text.

Biomedical Optics EXPRESS

The corpus callosum primarily comprised of axon fibers with encapsulated thin myelin sheaths was also imaged and analyzed as shown in Fig. 3. Even though the scattering power in the corpus callosum is similar to that in the olfactory bulb (Fig. 2), the μ_s is about four times lower in corpus callosum. It can be explained by the analysis result of Fig. 2 that shows μ_s of the region containing axon fibers has lower value than the region containing cell bodies. Thus, we also found that μ_s is significantly lower in NIR region in corpus callosum in the graph of Fig. 3(c). Specifically, μ_s value was measured to be 1.32 at 900 nm, which is 5.08 times lower than that measured at 550 nm.

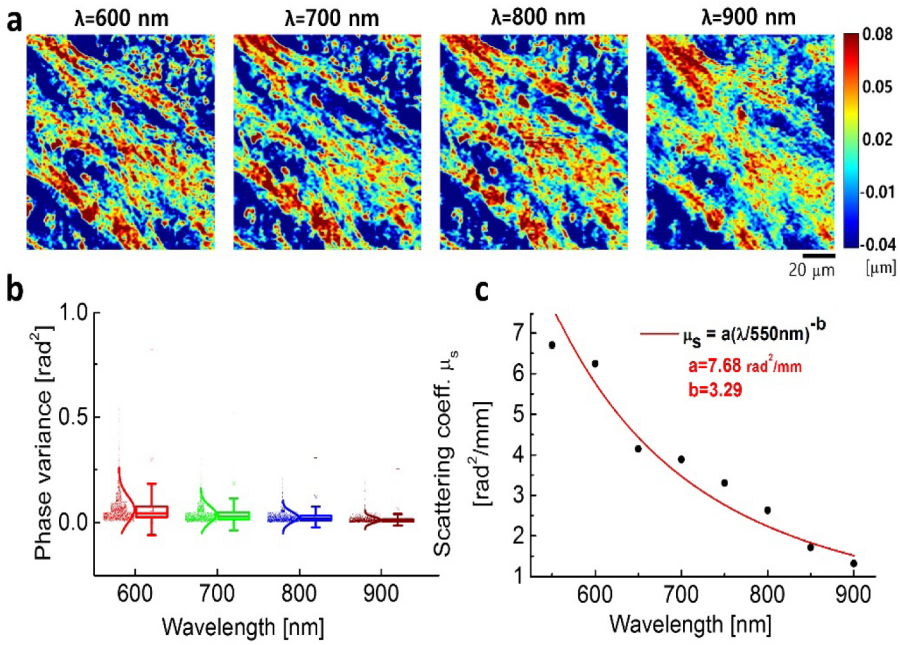

Fig. 3. MS-DPM images of the corpus callosum (a) and the corresponding graphs of phase variance (b) and scattering coefficient (c).

The other important scattering property is the anisotropy factor, g. The anisotropy factor is defined as the mean cosine of the scattering when the scattered light spreads more isotropically. Initially, the scattering angle, and thus decreases intensity maps [Figs. 4(a) and 4(d)] were obtained by applying the Fourier transform to the image fields corresponding to the olfactory bulb shown in Fig. 2 and corpus callosum shown in Fig. 3. In order to analyze the behavior of anisotropy at the different wavelengths, we normalized the magnitude squared of the Fourier transform to obtain the probability density map of the angular scattering intensity [23, 24] [see Figs. 4(a) and 4(d)]. From this result, we show that the scattering intensity is broader for longer wavelengths, particularly in the corpus callosum. The scattering intensity is plotted as function of scattering angle in Figs. 4(b) and 4(e). The change in the angular scattering intensity associated with the corpus callosum was analyzed in more detail. Specifically, we found that the intensity profile in the range of 0-10° is strongly dependent on wavelength. The curve corresponding to 900 nm wavelength is easily differentiated from other wavelengths, as the intensity is high in the range of 0-2°, but much lower in the range of 2-10°. It means that anisotropy in this range is higher, i.e., the scattering more peaked forward at longer wavelength. At high scattering angles, the intensity increases for longer wavelengths. Considering the entire range of angles captured by the objective lens, 0-56°, anisotropy becomes smaller at longer wavelength for all the regions.

Biomedical Optics EXPRESS

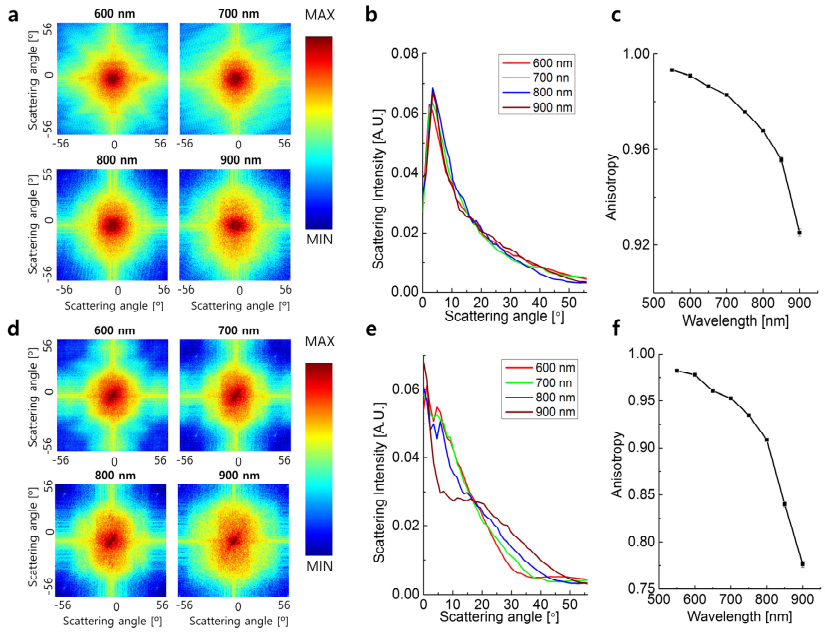

Fig. 4. Analysis of anisotropy vs. wavelengths in brain tissue using MS-DPM data: olfactory bulb (a-c) and corpus callosum (d-f). The angular scattering intensity (a, d), graphs of scattering intensity as a function of scattering angle (b, e), and anisotropy graph as a function of wavelength (c, f).

Following this intuitive observation, the anisotropy factor can be quantified using scattering-phase theorem as [19]

$$g = 1 - \frac{1}{2k_0^2} \frac{\langle \left| \nabla \left[\varnothing(r) \right] \right|^2 \rangle_r}{\langle \Delta \varnothing^2(r) \rangle_r^2},$$

where k_0 is the incident wave vector, and $\nabla[\varnothing(r)]$ is the phase gradient. k_0 was calculated by $2\pi n_0/\lambda_0$. n_0 and λ_0 are the average refractive index and the average wavelength of light in the brain tissue, respectively. This equation indicates that the anisotropy factor is not only related to the scattering coefficient, but also the phase gradient that has a relation with a tilt in the direction of propagation. The result shows that the anisotropy factor decreases at longer wavelengths, with an abrupt change at 800-900 nm [Figs. 4(c) and 4(f)]. The anisotropy factor is higher than 0.9 in the olfactory bulb for 900 nm, but lower than 0.8 in corpus callosum.

Thus, based on these results, wavelengths longer than 900 nm wavelength can facilitate the visualization of deeper tissue regions, especially for the fiber tracts in the brain. This is in agreement with previous reports [25–27]. During our analysis, the absorption coefficient (μ_a) was ignored because μ_s is typically much larger than μ_a. Even though, μ_a increases around the wavelengths of 900 nm due to the adsorption in lipid, absorption is less significant than the scattering coefficient [14, 22].

In order to better observe this effect, we tested 6, 10 and 14 μm thick brain tissue sections using three different wavelengths of 560, 638, and 752 nm, as shown in Fig. 5. In this experiment, the size of the image was 75 × 75 μm^2 (1500 × 1500 pixels) and pixel resolution was 50 nm. For 560 nm wavelength, the morphology of cells is difficult to recognize due to

Biomedical Optics EXPRESS

the high phase fluctuation, i.e., high scattering coefficient. On the other hand, at 752 nm, the morphology is much more identifiable.

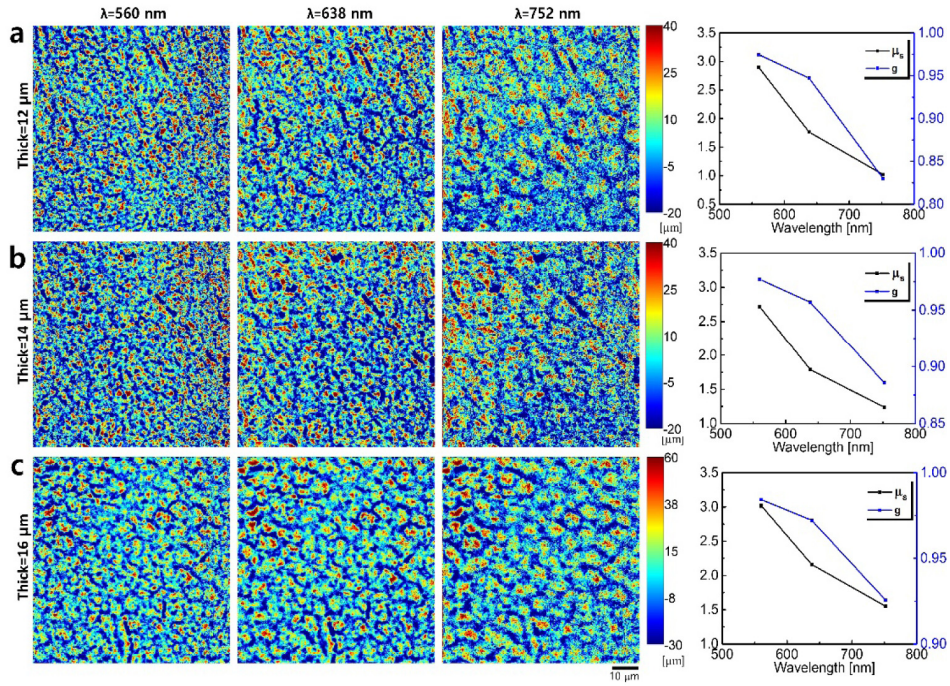

Fig. 5. MS-DPM images of brain tissue of thickness 12 μm (a), 14 μm (b), and 16 μm (c), and corresponding graphs of scattering coefficient and anisotropy as a function of wavelength.

4. Discussion and conclusions

In summary, we developed MS-DPM, which can provide comprehensive morphological information from brain tissue at various wavelengths. To confirm the feasibility of MS-DPM, different spectral bands were used for illumination and the results were compared and quantitatively analyzed in terms of the scattering coefficient (μ_s) and anisotropy factor (g). We found that scattering is reduced at longer wavelength so that MS-DPM contrast at longer wavelength is improved for delineating the structures especially in thicker tissue. To better understand the scattering in the brain tissue, we performed experiments for different regions in the brain, namely the olfactory bulb and corpus callosum, which mainly contains primarily cell bodies or myelin fibers, respectively. Our results reveal the strong spatial inhomogeneity of the brain tissue scattering properties. In addition, particularly in the region of 700-900 nm, lower μ_s and g exhibit significantly weaker scattering. Therefore, MS-DPM is a very promising tool for use in neuroscience research, especially organotypic culture, in which thick brain slices are used.

Funding

2016 Research Fund (1.160060) of UNIST (Ulsan National Institute of Science and Technology); Institute for Basic Science (IBS-R020-D1); and [EAGER, EBICS].

Acknowledgment

We would like to thank CheMyong J Ko and Sumin Kim for providing the mouse brains. We are grateful to Sungho kim for their technical assistance.